Article:

Mei, Jidan, Pei, Yuqing, Zakharov, Yury orcid.org/0000-0002-2193-4334 et al. (2 more authors) (Accepted: 2020) Improved underwater acoustic imaging with non-uniform spatial resampling RL deconvolution. IET Radar, Sonar & Navigation. ISSN 1751-8792 (In Press)

IET Research Journals

Research Article

ISSN 1751-8644
doi: 0000000000
www.ietdl.org

Improved underwater acoustic imaging with non-uniform spatial resampling RL deconvolution

Jidan Mei^{1,2,3}*, Yuqing Pei*^{1,2,3}*, Yuriy Zakharov*^{4}*, Dajun Sun*^{1,2,3*}*, Chao Ma*^{1,2,3}

[1] *Acoustic Science and Technology Laboratory, Harbin Engineering University, Harbin, China*
[2] *College of Underwater Acoustic Engineering, Harbin Engineering University, Harbin, China*
[3] *Key Laboratory of Marine Information Acquisition and Security (HEU), Ministry of Industry*
[4] *Department of Electronic Engineering, University of York, Heslington, York YO10 5DD, United Kingdom*
** E-mail: sundajun@hrbeu.edu.cn*

Abstract: Underwater acoustic imaging (UAI) can be utilized to observe the spatial distribution of a near-field sound source. The image quality depends on the resolution and sidelobe level of conventional beamforming. The linear array based UAI can be considered as deconvolution of a two-dimensional point spread function shift-variant model. The performance of UAI can be improved via innovative deconvolution algorithms. In this study, a non-uniform spatial resampling Richardson-Lucy (RL) fast algorithm is designed in which the amount of samples is determined by the power of the UAI output. This allows for a significant decrease in the number of samples compared to the traditional RL algorithm with similar positioning accuracy. Computer simulations and sea trials are performed to validate the effectiveness and feasibility of the proposed method.

1 Introduction

The underwater acoustic imaging (UAI) [1-2] is a technique for passive positioning of sound sources in which the source distribution can be determined via conventional beamforming (CBF). The near-field model considers sound waves as spherical waves. For acoustic waves, if the distance from the sound source to the center of the array is less than $(W^2/4\lambda)$ [3], it can be considered as a near-field sound source, where W is the maximum aperture width and λ is the wavelength. In the near-field, CBF uses spherical wave compensation. The positioning accuracy depends on the resolution and sidelobe level of CBF. High-resolution methods such as MVDR [4], MUSIC [5], and ESPRIT [6] are available for UAI applications, but are limited in performance due to their sensitivity to the underwater environment and array errors. Deconvolution algorithms have been widely used for sound source positioning [7-8], radar signal processing [9], image processing [10-11], and direction-of-arrival (DOA) estimation [12-13]. They outperform other conventional methods in terms of spatial resolution, sidelobe level, and robustness to the underwater environment. In this study, we seek to further improve the performance of UAI via deconvolution. The passive positioning of an underwater near-field sound source is similar to that of an aeroacoustic source, but does present significant differences. In general, the passive positioning of underwater sound sources is characterized by low signal-to-noise (SNR) ratio, large array position errors, and wide scanning areas. The underwater environment is highly complex and features multi-path phenomena. The relatively low SNR introduces complications in the deconvolution passive positioning process. It is difficult to ensure the precise placement of the underwater measurement array; thus, the position errors of the array are large and the robustness of the algorithm must be extremely high to ensure accurate positioning. Measurements of the noise radiated by moving ships must be carried out across a wide scanning area. The UAI measurement is a near-field problem, the point spread function (PSF) shift-invariant deconvolution cannot be used, and the moving ship sound sources cannot be fixed in some special measurement area where deconvolution can be approximated to the PSF shift-invariant model for measurement like some air sound source measurement.

Some deconvolution algorithms can be directly applied to deal with the PSF shift-variant model, such as the deconvolution technique for the mapping of acoustic sources (DAMAS) [14], non-negative least squares (NNLS) [15], CLEAN [16], and Richardson-Lucy (RL) algorithm [17-19]. However, these algorithms require large amounts of computation for deconvolution of the two-dimensional (2D) PSF shift-variant model. It is possible to transform the PSF shift-variant model into an approximate shift-invariant model by coordinate transformation methods [10] or by adding certain constraints to the measurement. For example, the measurement range can be limited to a small range of angles and the image can be divided into several segments, for which one can assume an approximate shift-invariant PSF [20-21]. After conversion to the PSF shift-invariant model, fast algorithms based on the Fast Fourier Transform (FFT) can be used to solve the problem (e.g., DAMAS2 [14], FISTA-DAMAS [22], FFT-NNLS [23], FFT-RL [24]). Unfortunately, in the underwater environment, it is difficult to establish a suitable mapping relationship to convert a PSF shift-variant model into a PSF shift-invariant model. DAMAS and NNLS are suitable for PSF shift-variant models, but their performance is not ideal at low signal-to-noise ratios (SNRs). CLEAN [25] is also suitable for the PSF shift-variant model, but it provides poor results for coherent sources. The RL algorithm has relatively good multi-target resolution performance and robustness at low SNR in addition to being suitable for the PSF shift-variant model [26].

In this study, we conduct underwater near-field sound source passive positioning based on the RL algorithm. The paper [27] compares the performance of 2D shift-variant RL algorithm in UAI with conventional and MVDR methods. The paper [28] proposes an algorithm for energy correction to improve the performance of the RL algorithm in locating sound sources near the image edge, and compares it with various deconvolution algorithms in UAI. According to [27, 28], the RL algorithm has better multi-target resolution and lower sidelobe level than other methods at low SNR. The original 2D RL method has a large computational burden, so a non-uniform spatial resampling RL fast algorithm is proposed to reduce the amount of calculation. First, we use a pre-calculated PSF dictionary to modify the conventional RL algorithm for dealing with the PSF shift-variant model. We then transform the 2D dictionary into a one-dimensional (1D) dictionary to simplify computations. Non-uniform sampling is performed on the scanning grid of an acoustic image to minimize the number of grid points. The resampling grid density is determined according to the energy distribution of the original acoustic image, which ensures that the areas with the sound source are densely sampled and important information is retained while the noisy background grid is sparsely sampled. This significantly reduces the computational burden compared to the original RL method without sacrificing the accuracy.

In Section 2, we present the basic principle and 2D convolution model of the UAI measurement. In Section 3, the RL deconvolution method is reviewed, and we propose a method to convert the 4D PSF dictionary into a 2D PSF dictionary, so that the 2D convolution can accordingly be simplified to the 1D convolution. In Section 4, a fast RL algorithm based on non-uniform spatial resampling is proposed. In Section 5 and 6, we conduct simulations and sea tests to validate the feasibility and effectiveness of the proposed method by comparing it with the original RL algorithm.

2 Basic theory and 2D convolution model of UAI measurement

2.1 Basic theory of UAI

Conventional UAI method is based on CBF, which uses spherical wave compensation model in the near-field. Fig.1 illustrates the test model. A diagram of the linear array with N elements and the element spacing d is shown in Fig. 1. We define a grid over the scanning plane with a fixed step size. By scanning over the grid points and using the near-field beamforming, the beam power output provides the acoustic image measurement; this yields the spatial acoustic source distribution map. The position of the sound source can be located according to the maximum intensity of the acoustic image. Here, we adopt a simplified 2D acoustic image model; we assume that the source depth is constant over the measurement area. We also assume that the source depth and array depth are known, and that the sound source and scanning point are in the same horizontal plane.

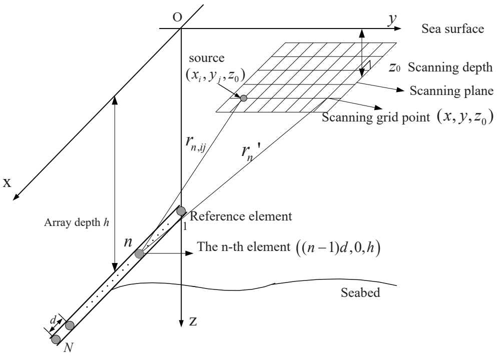

Fig. 1: Acoustic image measurement geometry [28, 29]

The array is positioned on the xoz plane and parallel to the x axis, the y coordinate of all array elements is 0. The coordinates of the n-th array element is $((n-1)d, 0, h)$. The broadband source spectrum can be divided into narrow bands and then acoustic images obtained for these bands averaged over frequency; the narrowband source model is therefore discussed here. The radiation signal of a narrow-band sound source at the position (x_i, y_j, z_0) is denoted as $s_{ij}(t)$ and the central angular frequency of the sound source is f_0. The received signal at the n-th element of the array can be approximately expressed as:

$$R_n(t) = \sum_i \sum_j A_{n,ij} s_{ij} \left(t - \frac{r_{n,ij}}{c}\right), \tag{1}$$

where $A_{n,ij}$ is the amplitude of the sound source signal received by the n-th array element from the (i,j)-th grid point, c is the underwater sound velocity, $r_{n,ij}$ is the distance between the sound source at the position (x_i, y_j, z_0) and the n-th element $((n-1)d, 0, h)$ given by

$$r_{n,ij} = \sqrt{(x_i - (n-1)d)^2 + {y_j}^2 + (z_0 - h)^2}, \tag{2}$$

r'_n is the distance from the scanning grid point (x, y, z_0) to the n-th array element $((n-1)d, 0, h)$ given by

$$r_n{}' = \sqrt{(x - (n-1)d)^2 + y^2 + (z_0 - h)^2}. \tag{3}$$

Scanning over all grid points in the scanning plane by the near-field CBF results in the beamformer output signal:

$$\begin{aligned} b(x,y,t) &= \sum_{n=1}^{N} R_n \left(t + \frac{r'_n}{c}\right) \\ &= \sum_i \sum_j A_{n,ij} s_{ij} \left(t - \frac{r_{n,ij}}{c} + \frac{r'_n}{c}\right) \end{aligned}, \tag{4}$$

where (x, y) represents the position of scanning grid point in the scanning plane. For narrow-band signals, the delay compensation can be replaced by the phase compensation, thus, this expression can be rewritten as:

$$b(x,y,t) = \sum_i \sum_j s_{ij}(t) \sum_{n=1}^{N} A_{n,ij} e^{-jk\left(r_{n,ij} - r'_n\right)}, \tag{5}$$

and the wave number is given by $k = 2\pi f/c$. The near-field beam power is given by

$$B(x,y) = \overline{|b(x,y,t)|^2}, \tag{6}$$

where "$\overline{(\cdot)}$" is the time average and "$|\cdot|^2$" is the square magnitude of the complex number.

2.2 2D convolution model of UAI

The near-field CBF beam power can be expressed as the array response $p(x, y\,|x_i, y_j\,)$ from a source located at point (x_i, y_j) to the steering position (x, y) times the source power, integrated over all possible source positions:

$$B(x,y) = \sum_i \sum_j q(x_i, y_j) p(x, y\,|x_i, y_j\,), \tag{7}$$

where $q(x_i, y_j)$ is the power of a narrow-band sound source at position (x_i, y_j). From (6), it follows that

$$\begin{aligned} B(x,y) &= \overline{|b(x,y,t)|^2} = \overline{\left| \sum_i \sum_j s_{ij}(t) \sum_{n=1}^{N} A_{n,ij} e^{-jk\left(r_{n,ij} - r'_n\right)} \right|^2} \\ &= \overline{\left(\sum_i \sum_j s_{ij}(t) \sum_{n=1}^{N} A_{n,ij} e^{-jk\left(r_{n,ij} - r'_n\right)}\right) \left(\sum_{i'} \sum_{j'} s_{i'j'}(t) \sum_{n=1}^{N} A_{n,i'j'} e^{-jk\left(r_{n,i'j'} - r'_n\right)}\right)^*} \\ &= \sum_i \sum_j \sum_{i'} \sum_{j'} \overline{s_{ij}(t) s^*_{i'j'}(t)} \left(\sum_{n=1}^{N} A_{n,ij} e^{-jk\left(r_{n,ij} - r'_n\right)}\right) \left(\sum_{n=1}^{N} A_{n,i'j'} e^{-jk\left(r_{n,i'j'} - r'_n\right)}\right)^* \end{aligned} \tag{8}$$

where "$()^*$" indicates conjugate of a complex number. There are cross terms between sound sources in this equation. When the sound sources are incoherent, the corresponding signals have independent random phases, and the cross terms vanish due to the averaging in time, meaning that only terms with $i = i', j = j'$, are non-zero. In this case, (8) can be approximately expressed as (7), where $q(x_i,y_j)=\overline{\left|s_{ij}(t)\right|^2}$. The source power matrix $\mathbf{q}$ is composed of powers of all sound sources in the measurement area. The matrix $\mathbf{q}$ represents the sound source location and its intensity. With a limited number of sound sources in the measurement area, the matrix $\mathbf{q}$ is sparse, $\mathbf{q}(x_i,y_j)=q_{ij}$, and the other values are zero. $p(x,y\left|x_i,y_j\right.)$ in the narrow-band case is expressed as:

$$p(x,y\left|x_i,y_j\right.)=\left|\sum_{n=1}^{N}e^{-jk\left(r_{n,ij}-r'_n\right)}\right|^2. \tag{9}$$

For sources located at different positions, the near-field beam patterns are different. We can use (9) to obtain near-field beam patterns for all grid points, thus creating a dictionary $\mathbf{p}$ of beam patterns.

If $p(x,y\left|x_i,y_j\right.)$ satisfies the following formula:

$$p(x,y\left|x_i,y_j\right.)=p(x-x_i,y-y_j), \tag{10}$$

we say that the PSF is shift-invariant, and

$$B(x,y)=\sum_i\sum_j q_{ij}p(x-x_i,y-y_j). \tag{11}$$

$B(x,y)$ is an acoustic image represented as a matrix $\mathbf{B}$ that can be expressed as the 2D convolution of the matrix $\mathbf{q}$ and the PSF matrix $\mathbf{p}$:

$$\mathbf{B}=\mathbf{q}**\mathbf{p}, \tag{12}$$

where "$**$" denotes the 2D convolution. The source power matrix $\mathbf{q}$ can be obtained by deconvolution of $\mathbf{B}$ and $\mathbf{p}$. In an ideal case, $\mathbf{q}$ is a set of 2D Dirac delta functions related to the source intensity and position.

For near-field acoustic image measurement using a horizontal line array, the PSF is shift-variant in space, i.e., $p(x,y\left|x_i,y_j\right.)$ does not satisfy (10), and $B(x,y)=\sum\limits_i\sum\limits_j q(x_i,y_j)p(x,y\left|x_i,y_j\right.)\neq\mathbf{q}**\mathbf{p}$. Equation (7) is a generalized convolution model or blurring model. The fast algorithms based on FFT cannot be used to solve the deblurring problem, because they are based on the shift-invariant model. The original RL deconvolution can be applied to PSF shift-variant model, but the original RL algorithm requires a high computational load. Therefore, below we present a fast RL deconvolution algorithm for the 2D PSF shift-variant model.

3 Deconvolution method

3.1 Review of original RL deconvolution

Equation (7) is a discrete expression of 2D convolution. The 2D convolution can be written in a general form as

$$\upsilon(\xi,\eta)=\int_{-\infty}^{+\infty}\int_{-\infty}^{+\infty}s(x,y)h(\xi,\eta\left|x,y\right.)\,dxdy, \tag{13}$$

where $h(\xi,\eta\left|x,y\right.)$ is the shift-variant PSF, $\upsilon(\xi,\eta)$ is measured data, and $s(x,y)$ is the source power; note that $s(x,y)$ and $h(\xi,\eta\left|x,y\right.)$ are nonnegative real functions. If $\upsilon(\xi,\eta)$ and $h(\xi,\eta\left|x,y\right.)$ are both known, then $s(x,y)$ can be obtained by RL deconvolution. The RL is a Bayesian-based iterative method which is widely used for deblurring in imaging applications [11]. The algorithm is derived from the Csiszar discrimination under the constraint that all probabilities are nonnegative [17] [18]. The RL algorithm aims to recover $s(x,y)$ given the measured data $\upsilon(\xi,\eta)$. The 2D RL solution is given by

$$s^{(r+1)}(x,y)=s^{(r)}(x,y)\int_{-\infty}^{+\infty}\int_{-\infty}^{+\infty}\upsilon(\xi,\eta)\frac{h(\xi,\eta\left|x,y\right.)}{\upsilon^{(r)}(\xi,\eta)}d\xi d\eta, \tag{14}$$

where

$$\upsilon^{(r)}(\xi,\eta)=\int_{-\infty}^{+\infty}\int_{-\infty}^{+\infty}h(\xi,\eta\left|x,y\right.)s^{(r)}(x,y)dxdy, \tag{15}$$

r denotes the iteration index, $s^{(r)}(x,y)$ denotes the r-th estimate of the input term, $\upsilon^{(r)}(\xi,\eta)$ denotes the r-th estimate of the measured data based on $s^{(r)}(x,y)$ and $h(\xi,\eta\left|x,y\right.)$, and the initial value is $s^{(0)}(x,y)=\upsilon(x,y)$.

Substituting (15) into (14), one obtains the RL solution given by

$$\begin{aligned}&s^{(r+1)}(x,y)=\\&s^{(r)}(x,y)\int_{-\infty}^{+\infty}\int_{-\infty}^{+\infty}\upsilon(\xi,\eta)\frac{h(\xi,\eta\left|x,y\right.)}{\int_{-\infty}^{+\infty}\int_{-\infty}^{+\infty}h(\xi,\eta\left|x,y\right.)s^{(r)}(x,y)dxdy}d\xi d\eta.\end{aligned} \tag{16}$$

The number of iterations can be predefined or they can be carried out until the difference between the r-th and (r+1)-th estimated source distributions is sufficiently small. The convergence of the RL algorithm has been proven in [11]. It is noted that the RL solution can be obtained by minimizing the Csiszar discrimination [11]

$$\lim_{r\to\infty}s^{(r+1)}(x,y)=\underset{q(x,y)}{\arg\min}\,L\left(\upsilon(\xi,\eta),\int_{-\infty}^{+\infty}h(\xi,\eta\left|x,y\right.)s\,(x,y)\,dxdy\right), \tag{17}$$

where $L\left(p(x),q(x)\right)$ is the Csiszar discrimination given by [30][31]

$$L\left(p(x),q(x)\right)=\int_{-\infty}^{\infty}p(x)\log\frac{p(x)}{q(x)}\,dx-\int_{-\infty}^{\infty}\left[p(x)-q(x)\right]dx. \tag{18}$$

The $L\left(p(x),q(x)\right)$ is an appropriate way to measure the discrepancy between two nonnegative functions. For the UAI measurement, $B(x,y)$, $p(x,y\left|x_i,y_j\right.)$ and $q(x_i,y_j)$ are nonnegative real functions, so that the original RL algorithm has a unique solution.

3.2 RL deconvolution for UAI

For the UAI measurement, the integral boundaries are limited by the measurement area. Assume the boundaries are $(x_{\min},x_{\max})$ and $(y_{\min},y_{\max})$. One can apply the original RL algorithm to the UAI and obtain the following solution:

$$\begin{aligned}&q^{(r+1)}(X,Y)\\&=q^{(r)}(X,Y)\int_{x_{\min}}^{x_{\max}}\int_{y_{\min}}^{y_{\max}}B(x,y)\frac{p(x,y\left|X,Y\right.)}{\int_{x_{\min}}^{x_{\max}}\int_{y_{\min}}^{y_{\max}}p(x,y\left|X,Y\right.)q^{(r)}(X,Y)dXdY}dxdy\\&=q^{(r)}(X,Y)\int_{x_{\min}}^{x_{\max}}\int_{y_{\min}}^{y_{\max}}B(x,y)\frac{p(x,y\left|X,Y\right.)}{B^{(r)}(x,y)}dxdy\end{aligned} \tag{19}$$

where (X,Y) is the sound source position. The grid(x_i,y_j), $i=1,2,...X_N,j=1,2,...Y_N$, is the discrete representation of (X,Y). X_N is the x-axis grid point in the measurement area, Y_N is the y-axis grid point in the measurement area. The initial value is $q^{(0)}(x,y)=B(x,y)$. Generally, it is difficult to solve the deconvolution of the shift-variant model because the PSF is variable. Under the conditions described in this paper, the PSF is predictable despite being shift-variant. The PSF dictionary can be pre-generated using (9). This method applies for any fixed array of known configuration and is not limited to linear arrays. For the 2D convolution model, the PSF dictionary is a multi-dimensional function because the near-field beam pattern $p(x, y\,|X, Y\,)$ corresponding to each assumed sound source position is a 2D image. It is necessary to generate near-field beam pattern for all positions in the measurement area to build the PSF dictionary.

For the 2D shift-variant model, the PSF dictionary for the whole measurement area is a 4D dictionary. In order to facilitate the solution, we propose a method to convert the 4D PSF dictionary into a 2D PSF dictionary; the 2D convolution can accordingly be simplified to the 1D convolution. The scanning points are discrete, so index variables v and u can be used to replace the index scanning values of the original 2D plane coordinates (X, Y) and (x, y). The 2D image storage can be converted into a 1D storage. The maximum values of v and u are equal to the total number of 2D plane scanning points $I = X_N \times Y_N$. Equations (7) and (19) can be written as follows:

$$B(u) = \sum_{v=0}^{V} p(u\,|v\,)q(v), \tag{20}$$

$$q^{(r+1)}(v) = q^{(r)}(v) \sum_{u=0}^{U} B(u) \frac{p(u\,|v\,)}{B^{(r)}(u)}, \tag{21}$$

where

$$B^{(r)}(u) = \sum_{v=0}^{V} p[u\,|v]q^{(r)}(v), \tag{22}$$

u represents the index of the scanning point position (x, y) and v represents the index of the sound source position (X, Y). $B(u)$ is a rearrangement of $B(x, y)$ in a row, and $q(v)$ is a rearrangement of $q(X, Y)$ in a row. In this process, the 2D matrix is converted into a vector. $p(u\,|v\,)$ is the near-field beam response in $u(x, y)$ of the source located at point $v(x, y)$, $p(u\,|v\,) = p(x, y\,|X, Y\,)$. A diagram in Fig.2 is used to describe the conversion process from the 4D PSF dictionary to a 2D PSF dictionary.

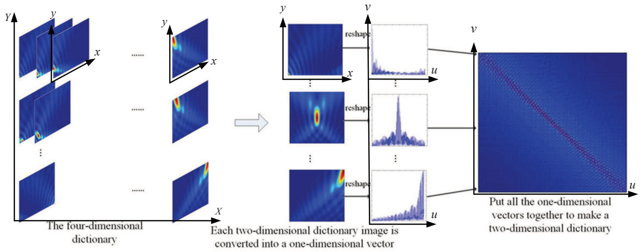

Fig. 2: Conversion process from the 4D PSF to a 2D PSF

As Fig.2 shows, the 2D PSF dictionary generation process is as follows. Firstly, use (9) to generate $p(x, y\,|x_i, y_j\,)$, which is a 2D image with $X_N \times Y_N = I$ pixels for each (x_i, y_j), and there are $X_N \times Y_N = I$ different (x_i, y_j), so we can get $X_N \times Y_N$ images, it can be seen as a 4D dictionary. Secondly, convert each 2D image into 1D storage vector of length I. The number of scalar values is the same as the number of the image pixels, they are just arranged differently. Thirdly, rearrange vectors by rows to form a 2D matrix $p(u\,|v\,)$, which is the 2D PSF dictionary.

Then we can use (21) to obtain the deconvolution result $q^{(r+1)}(v)$. Cutting $q^{(r+1)}(v)$ into Y_N segments at every X_N point, and then rearranging them into a 2D matrix by row, $q^{(r+1)}(X, Y)$ can be obtained.

Doppler frequency shifts occur in a fast-moving craft, which change the frequency of the source. When measuring a fast-moving craft, the near-field CBF beam power and the PSF dictionary all should be obtained according to Doppler shifted frequency, and then the deconvolution process is performed to ensure that the frequency relationship between the beam power and the PSF dictionary correspond to each other. This can avoid mismatches. During processing, one doesn't need to know the original frequency. However, if the PSF dictionary is still pre-stored according to the original frequency, and the deconvolution processing is performed on the near-field CBF beam power after the Doppler distortion, there will be a mismatch and the side-lobe level of the deconvolution will increase. For passive UAI, the original frequency of the source radiation is unknown, and the frequency after the Doppler distortion of the source signal can be obtained according to the spectrum analysis, and then all processing can be performed according to this frequency. The broadband signal processing is the same, if the frequency bands of beampower and PSF dictionary correspond to each other.

4 Fast RL algorithm based on spatial resampling

The UAI is used to describe the spatial distribution of sound sources. It is based on discrete scanning of near-field by CBF. A denser scanning grid corresponds to higher resolution. In the underwater sound source localization, the measurement area is generally very large due to the wide distribution of sources, for example the noise radiated underwater by a moving ship. A large merchant ship may have multiple noise sources, such as propeller noise, engine noise and vibration noise. They are in different parts of the ship and may be distributed over tens of meters. The ship is moving during the measurement. Thus a wider measurement area is needed. Consider a 100m×100m measurement area as an example. If the grid step is 1m, the number of grid points is 10^4 and the corresponding number of pre-stored PSF dictionary elements is 10^8. If the sound source location resolution is $(1/E)$m, the number of elements in the PSF dictionary reaches $E^4 \times 10^8$. The number of grid points has a substantial impact on the calculation process. Reducing the number of grid points is the direct approach to accelerate the computation. However, for a measurement area, reducing the number of grid points by increase the grid step size also reduces the measurement resolution thus affecting the positioning accuracy.

This paper presents a fast RL deconvolution method based on non-uniform spatial resampling. The resampling grid density is dependent on the energy distribution of the original UAI. High-energy areas are sampled densely and low-energy areas are sampled sparsely. This allows the area with the sound source to be sampled with high resolution while retaining the important information. The noisy background area is then sparsely sampled. After resampling, the computational burden is significantly reduced due to reduction of the number of scanning points. The measurement area of UAI is divided into multiple areas $M_1, M_2, ...M_i$ with different sampling rates. The sampling rate in different areas is set based on energy of the original UAI. The specific process is as follows.

The intensity of $B(x, y)$ reflects the energy of UAI at (x, y). Different energy thresholds D_i are set according to the intensity of $B(x, y)$. Scan points (x, y) can be divided into sets with different sampling density f_i:

$$\begin{cases} (x, y) \in M_1, \text{if} D_2 < B(x, y) \le D_1 \\ (x, y) \in M_2, \text{if} D_3 < B(x, y) \le D_2 \\ \vdots \\ (x, y) \in M_i, \text{if} B(x, y) \le D_i \end{cases}, \tag{23}$$

where D_1 represents the maximum intensity of the acoustic image, $D_1 > D_2 > \ldots > D_{i-1}$. To simplify the computation process, $B(x, y)$ is written as the 1D vector $B(u)$. Let the acoustic image obtained after resampling be $B(u')$, the non-uniform resampling is illustrated in Fig.3.

The parameter k_i is the grid sampling interval in the i-th area, which means that one point is taken for every k_i original points in this area, $k_i = 1/f_i$. The parameter k_i must be integer, and the larger D_i, the smaller k_i is. The non-uniform spatial resampling process

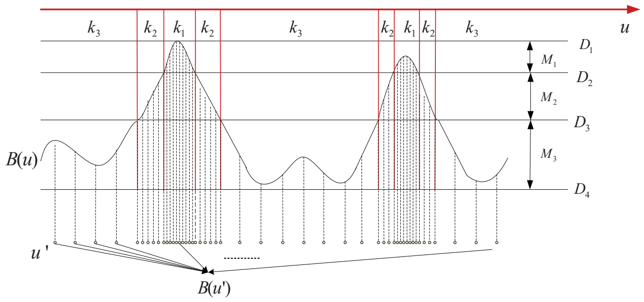

Fig. 3: The process of non-uniform spatial resampling

can be expressed as:

$$B(u') = re\left(B(u)\right), \tag{24}$$

where $re\left(\cdot\right)$ means non-uniform spatial resampling, (24) means a part of the $B(u)$ is decimated to form a resampled acoustic image $B(u')$ according to the rule shown in Fig.3. u' represents the decimated value of u, so u' is a subset of u, and u' is non-uniform. To ensure the appropriate resolution of the sound source, we let $k_1 = 1$ in the area M_1. That means that the resampled UAI has the same grid step with the original UAI in this area. The other $k_i > 1$ and $k_1 < k_2 < \cdots < k_i$.

The computations can be reduced by adjusting D_i. The RL deconvolution iteration after non-uniform spatial resampling is converted into:

$$q^{(r+1)}(v) = q^{(r)}(v)\sum_{u'} B(u')\frac{p(u'\,|v\,)}{B^{(r)}(u')}, \tag{25}$$

where $p(u'\,|v\,) = re\left(p(u\,|v\,)\right)$ represents resampling the u dimension of the PSF dictionary $p(u\,|v\,)$, which means that only $p(u\,|v\,)$ corresponding to u' are chosen to form a new resampling dictionary

$$B^{(r)}(u') = re\left(B^{(r)}(u)\right) = \sum_{v=1}^{V} p[u'\,|v\,]q^{(r)}(v), \tag{26}$$

$$q^{(r+1)}(v) = q^{(r)}(v)\sum_{u'} B(u')\frac{p(u'\,|v\,)}{\sum\limits_{v=1}^{V} p[u'\,|v\,]q^{(r)}(v)}. \tag{27}$$

We compared (16), (19), (21), and (27) to analyze the similarities and differences between the proposed spatial resampling algorithm and the original RL algorithm. The integral range of the original deconvolution in (16) is $(-\infty, \infty)$. In (19), the boundary is changed into a finite continuous boundary due to the limited measurement area. When the measurement area contains the main information of the source (mainlobe and main sidelobe), the truncated boundary has little effect on the source measurement. Equation (21) is only a 1D expression of (19); the two are equivalent. Essentially, from (21) to (27), only the integration area is further changed. This change is different from the truncation of boundaries. Rather, it divides the integral region into non-uniform regions. In the iterative integration, some points with low original output energy in the region defined in (21) are removed so that the computation is minimized while retaining important information. On the whole, the non-uniform spatial resampling RL algorithm only changes the convolution integral area; it creates a non-uniform and non-regular integral area but does not alter the computation process of the iterative algorithm itself.

It needs to be emphasized that only the u-axis of the PSF dictionary $p(u\,|v\,)$ and the original UAI $B(u)$ have been resampled in the iterative computation [see (27)], the v-axis of the PSF dictionary $p(u\,|v\,)$ has not been resampled. So, the grid density of the deconvolution output remains unchanged. This means that the range and the number of grid points of the resampling RL is the same as in the original RL and CBF. The process can be summarized as follows.

- The near-field CBF algorithm is used to scan the measurement area at a fine grid to obtain an acoustic image;
- The acoustic image is divided according to the threshold values for the image intensity. Non-uniform spatial resampling is performed according to the division;
- The u axis of PSF dictionary and conventional acoustic image are resampled. They are subjected to RL deconvolution. Then, the deconvolution results can be obtained as in (27).

5 Numerical simulation and analysis

5.1 Comparison of acoustic images

We ran simulations to compare the performance of the original RL algorithm and the spatial resampling RL algorithm under three conditions: single source, two sources with equal intensities, and two sources with different intensities. The measurement model is shown in Fig. 1. The number of array elements is $N = 21$, the spacing is 2 m, the x-range of the scanning area is [-10m, 10m], and the y-range is [10m, 40m]. We assume that the sound source and the array are in the same xy-plane. The source frequency is 600 Hz, the noise frequency bandwidth is 400 Hz-800 Hz, and the SNR is 15 dB (in-band signal to noise ratio). During the processing, it is assumed that the source frequency is unknown. We let the position of the sound source in the single source simulation be (0m, 26m) and the position of the sound source in the two source simulations be (-1m, 26m) and (0.6m, 22.8m). The SNR difference between two sources of unequal intensities is 3 dB. The number of deconvolution iterations is set to 200. Subsets of non-uniform spatial resampling were divided after the original acoustic image was normalized. The partition parameters are listed in Table 1.

Table 1 Subsets of spatial resampling

i	Threshold D_i	k_i
1	0dB	1
2	-3dB	7
3	-10dB	15
4	-15dB	30

Table 2 shows the number of scan points in the two RL methods for a single source and two sources with a uniform grid sampling interval of 0.2m×0.4m (the sampling interval of x-axis is 0.2m, and the interval of y-axis is 0.4m) as an example.

Table 2 Comparison of the number of scan points

Sampling method Sound sources	Uniform sampling	Non-uniform sampling
Single source	7676	737
Two sources with unequal intensities	7676	930

Table 2 shows that the number of non-uniform grid points depends on the number of sound sources. The energy distribution area of sound sources is larger when there are multiple sound sources. In general, the non-uniform sampling allows reduction in the computational complexity by an order of magnitude. The comparison of images obtained by the RL and non-uniform sampling RL deconvolution methods is provided in Fig. 4 and Fig. 5.

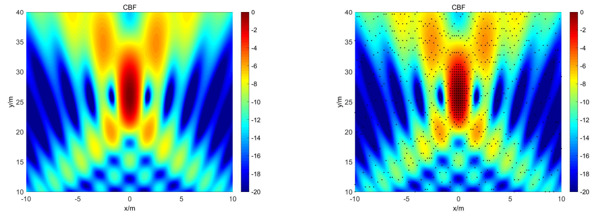

(a) Conventional beamforming with the uniform sampling

(b) Conventional beamforming with the non-uniform sampling

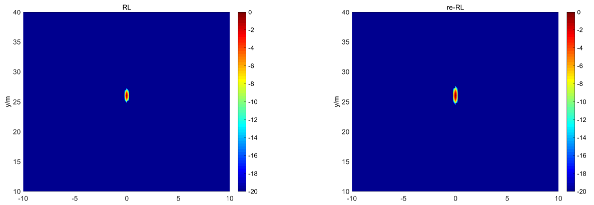

(c) RL method with the uniform sampling

(d) Fast RL method (non-uniform sampling)

Fig. 4: Comparison of acoustic images obtained from the original sampling (a, c) and after the resampling (b, d) for the case of the single source

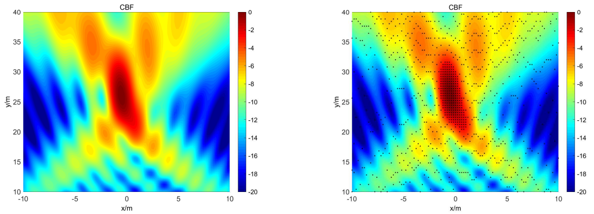

(a) Conventional beamforming with the uniform sampling

(b) Conventional beamforming with the non-uniform sampling

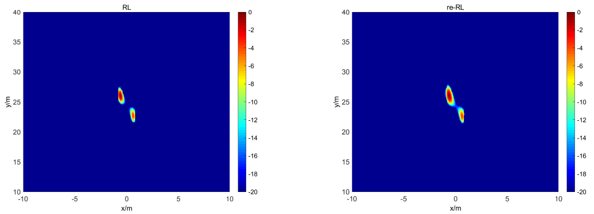

(c) RL method with the uniform sampling

(d) Fast RL method (non-uniform sampling)

Fig. 5: Comparison of acoustic images obtained from the original sampling (a, c) and after the resampling (b, d) for the case of two sources with different intensities

Fig.4 and Fig.5 show that compared with the original CBF acoustic image, the RL algorithm and non-uniform spatial resampling RL algorithm provide significantly improved images. The images obtained by the non-uniform spatial resampling RL algorithm are very close to images obtained by the original RL algorithm in terms of mainlobe area of near-field beamforming, sidelobe level, and resolution, but the non-uniform spatial resampling RL algorithm requires significantly less computational effort due to a smaller number of grid points. The mainlobe area is defined as shown in Fig.6 (a) and it is measured in m^2. It refers to the area surrounded by the boundary formed by the main peak drop of 3dB in the case of a single sound source. For example, the area surrounded by the black curve in Fig.6 (b) is the mainlobe area of CBF UAI. It is used to describe the resolution of the UAI method on a two-dimensional plane.

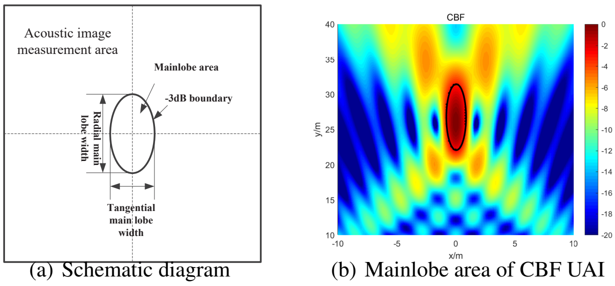

(a) Schematic diagram

(b) Mainlobe area of CBF UAI

Fig. 6: Schematic diagram of two-dimension mainlobe widths

5.2 *Analysis of mainlobe area*

We also assessed the resolution of the proposed algorithm based on the mainlobe area. The simulation conditions (except SNR) are the same as those in Section 5.1.

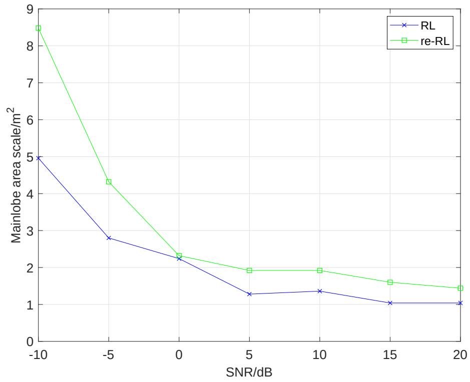

Fig. 7: Mainlobe area of RL versus spatial resampling RL algorithm

As shown in Fig.7, with the same number of iterations (200), the mainlobe area of the spatial resampling RL algorithm is slightly higher than that of the original RL algorithm (though very similar). When SNR is greater than 0 dB, the two are very close. The spatial resampling RL algorithm does not significantly reduce the focusing performance compared to the original algorithm.

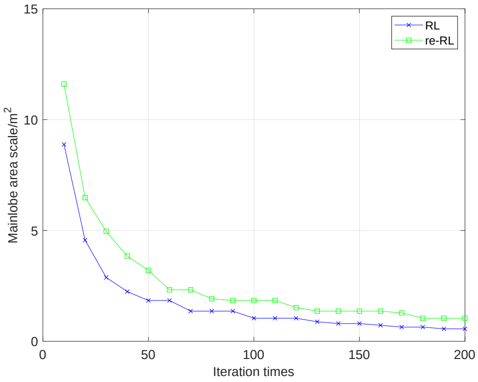

Fig. 8: The mainlobe area of RL algorithm and spatial resampling RL algorithm against iterations

Fig.8 compares the mainlobe area of RL algorithm and spatial resampling RL algorithm with various numbers of iterations. The simulation conditions (except the number of iterations) are the same as those in Section 5.1. The mainlobe area of both methods gradually decreases as the iterations progress, which indicates that the spatial resampling RL algorithm is still convergent. In the case of the same SNR (15 dB), after 50 iterations, the mainlobe area of the spatial resampling RL algorithm is very close to that of the RL algorithm. In effect, the two algorithms perform similarly.

5.3 *Comparison of spatial resolution limits*

The resolution is defined by the minimum separation distance between distinguishable point sources. This section discusses the resolutions of the CBF, RL, and spatial resampling RL algorithms. It needs to be emphasized that only one dimension of the PSF dictionary and the original UAI have been resampled in the iterative computation (see (27)), another dimension of the PSF dictionary has not been resampled. So, the grid density of the resampling RL output remains unchanged. That means the range and the number of grid points of the resampling RL algorithm is the same as for the original RL and CBF. The resampling UAI is only used to calculate the resampling deconvolution. Because its grid points are non-uniform, we do not use it to observe the spatial distribution of the sources. Suppose that two single frequency sources of equal intensity are located at (x, y_0) and $(-x, y_0)$. Gradually increasing x, we reach the event when the two peaks are just separated, then $2x$ is the spatial resolution limit along the x coordinate.

Simulation conditions: The number of array elements is $N = 21$, the spacing is 2 m, the range interval for y_0 is [5m, 40m]. The signal frequency is 600 Hz, the noise frequency bandwidth is 400 Hz-800 Hz, and the SNR is 15 dB. The number of deconvolution iterations is set to 200. The partition parameters that we adopted are listed in Table 1.

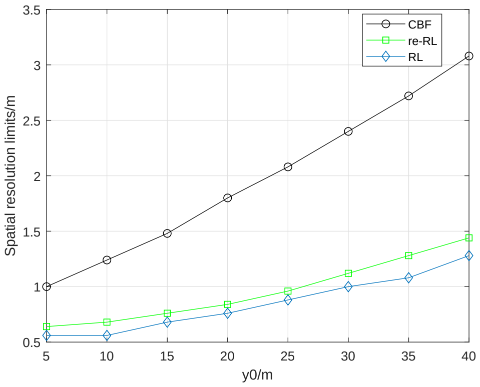

Fig. 9: Spatial resolution limits

As shown in Fig.9, the limit resolution of the three algorithms improves as y_0 is reduced. The limit resolution of the RL and spatial resampling RL algorithms are very close. The RL resolution varies from 0.56 m to 1.28 m, whereas the resolution of the spatial resampling RL algorithm varies from 0.64 m to 1.44 m, and that of the CBF varies from 1 m to 3.08 m. The x-direction limit resolution of the RL and spatial resampling RL algorithms is significantly better than that of the CBF.

5.4 *Comparison of Main-to-side lobe ratio*

We now compare the main-to-side lobe ratio of the CBF, RL, and spatial resampling RL algorithms as shown in Table 3. Other simulation conditions (except SNR) are kept the same as those in Section 5.1 for the single source.

Table 3 and Fig.10 show that for the RL and spatial resampling RL algorithms at SNR≥10dB, the sidelobe level is extremely low and the main-to-side lobe ratio is less than -70dB. When SNR is higher than 10dB, the impact of noise on the conventional UAI is very small. From Fig.10, we can find that the main-to-side lobe ratio of the CBF is almost unchanged when SNR is higher than 10dB. That means the UAI is very close to the noise-free ideal UAI, and the deconvolution is close to the noise-free ideal model, so the sidelobe is very low after RL deconvolution. The main-to-side lobe ratio of the spatial resampling RL algorithm is slightly lower than that of the original RL algorithm when SNR is between -10 dB and 5 dB, which is due to the use of fewer points in the noise background.

Table 3 Main-to-side lobe ratio (dB) at different SNR

Algorithm \ SNR/dB	-10	-5	0	5	10	15	20
CBF	-2.68	-4.11	-5.01	-5.21	-5.41	-5.44	-5.45
RL	-5.06	-5.17	-6.87	-8.83	<-70	<-70	<-70
re-RL	-5.41	-6.93	-9.99	-11.35	<-70	<-70	<-70

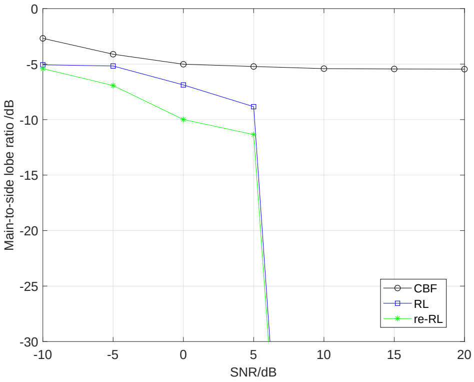

Fig. 10: Main-to-side lobe ratio

5.5 *Analysis of positioning errors*

We now compare the positioning accuracy of the fast RL algorithm and the original RL algorithm. The deconvolution acoustic image and real sound source distribution standard deviation σ_s is defined as:

$$\sigma_s = \frac{1}{V}\sqrt{\sum_{v=1}^{V}\left(q^{(r)}(v) - q_{real}(v)\right)^2}, \qquad (28)$$

where q_{real} is the real source power distribution given by

$$q_{real}(v) = \sum_{ij} A_{ij}^2 \cdot \delta(v - v_{ij}), \qquad (29)$$

A_{ij}^2 is the power of the source at (x_i, y_j, z_0); v_{ij} represents the 1D index of the sound source position (x_i, y_j, z_0). The value of σ_s reflects the recovery degree of the deconvolution algorithm to the location of a sound source as a Dirac delta function. Smaller σ_s indicates stronger similarity between the deconvolution acoustic image and the real sound source image, in addition to better positioning accuracy, smaller sidelobes. The σ_s-curves of the two deconvolution algorithms are shown in Fig.11. The sound source position in this case is (0m, 26m) and other simulation conditions (except the number of iterations) are the same as those in Section 5.1 for the single source.

Fig.11 shows σ_s against the number of iterations. As the iterations progress, σ_s of the two RL algorithms decreases; this further indicates that the spatial resampling RL algorithm converges. The positioning errors of the spatial resampling RL algorithm are consistently close to that of the RL algorithm.

5.6 *Analysis of robustness*

We took the position errors of the array elements as an example to illustrate the robustness of the proposed method. Here, assume that

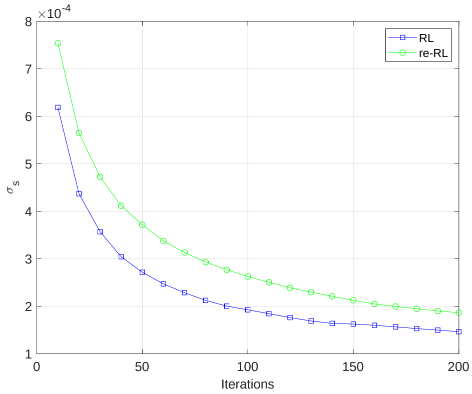

Fig. 11: Comparison of σ_s-curves

the ideal position of the m-th array element is (x_m, y_m, h) and the actual position is (x'_m, y'_m, h). The error standard deviation of the position in the x-direction and y-direction is 0.06d and d is the spacing between the array elements. Other simulation conditions are the same as those in Section 5.1. The positions of real and ideal array elements are shown in Fig.12(a). We observe changes in the mainlobe area, sidelobe level, and positioning error, the results are shown in Fig.12(b), Fig.12(c), and Fig.12(d).

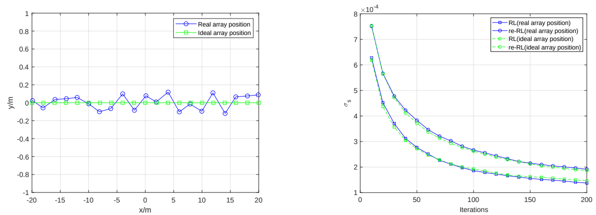

(a) Array element positions (b) Comparison of σ_s-curves

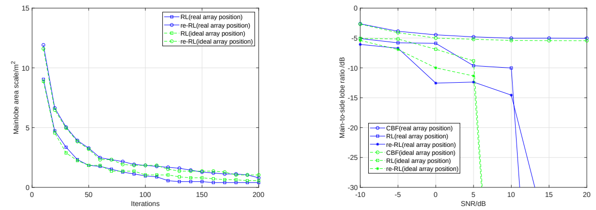

(c) Relation between iteration times and mainlobe area (d) Relation between SNR and main-to-side lobe ratio

Fig. 12: Performance of acoustic image measurement with array position errors

Under the simulation condition of Fig.12(a), as can be seen from Fig.12(b), the position of the sound source is very close to that of the ideal array without errors. The positioning error of the fast algorithm is slightly higher than that of the original RL algorithm. As can be seen from Fig.12(c), the mainlobe area of the source is very close to that of the ideal array without errors. In Fig.12(d), the sidelobe level of the two RL algorithms is slightly higher than that of the ideal array without errors. This is because the position error of array elements will change the shape of UAI, and then the PSF dictionary will have a discrepancy with the real one. However, since both the original UAI and PSF dictionary generation are based on CBF, CBF has the characteristics of high robustness and is not sensitive to small position errors of the array elements, so it can still maintain good performance after deconvolution processing.

6 Sea test

We further evaluate the performance of the acoustic imaging on sea test data collected in the Bohai Sea area of China. An uniform linear array with 10 elements was placed on the seabed with 5 m spacing making a total array length of 45 m (Fig. 13). The array axis deviates from the north direction by about 13.5°. The position of each array element was determined by high-precision GPS. The depth of the No. 9 array element, according to a pressure sensor, was about 25.25 m. The No. 1 array element had a drop of about 5 m with respect to the No. 10 element due to the inherent unevenness of the sea floor, as shown in Fig. 14.

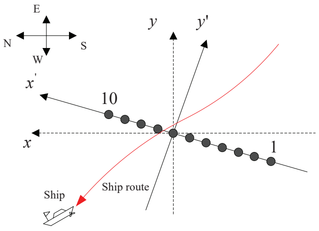

Fig. 13: Sea test layout

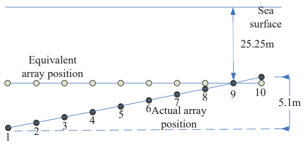

Fig. 14: Side view of the array

The depth error was corrected during the data processing. The single source test ship is a fast-moving small motorboat, and the dual-source ship is a catamaran which has two propellers. The sound was emitted by the ship propeller. The source depth is about 1m. We set the scanning plane at a depth of 1m. The main noise frequency band of the propeller sound source was located during the test with a default source scanning depth of 1 m.

The processing results for the CBF, RL, and re-RL algorithms with 100 deconvolution iterations for three different moving source positions of a single source are shown in Fig.15. The signal processing frequency range in this case was from 500Hz to 1500 Hz. The broadband source spectrum was divided into narrow bands and then acoustic images and PSF dictionaries obtained for each narrow band. The broadband UAI was obtained by averaging all the narrow bands acoustic images. The PSF dictionary is obtained by averaging all the narrow bands PSF dictionaries. It was divided into 100 narrow bands from 500 to 1500 Hz, each narrow bandwidth is 10 Hz. The partition parameters are listed in Table 4.

Table 4 Subsets of spatial resampling for the experiment with a single source

i	Threshold D_i	k_i
1	0dB	1
2	-2dB	3
3	-5dB	12
4	-12dB	21

Table 5 shows the number of scan points in the two-grid sampling RL methods for three different moving source positions with a uniform grid sampling interval of 0.25 m×0.5m (the sampling interval over the x-axis is 0.25m, and over the y-axis is 0.5m.) as an example.

Table 5 Comparison of scan point quantities

Sampling method Sound positions	Uniform sampling	Non-uniform sampling
Position 1	10201	700
Position 2	10201	662
Position 3	10201	686

As shown in Fig.15, the sidelobe level of the RL method and re-RL algorithms are significantly lower than that of the conventional acoustic image. The mainlobe area of the former two methods are also significantly smaller. The mainlobe area of the re-RL algorithm

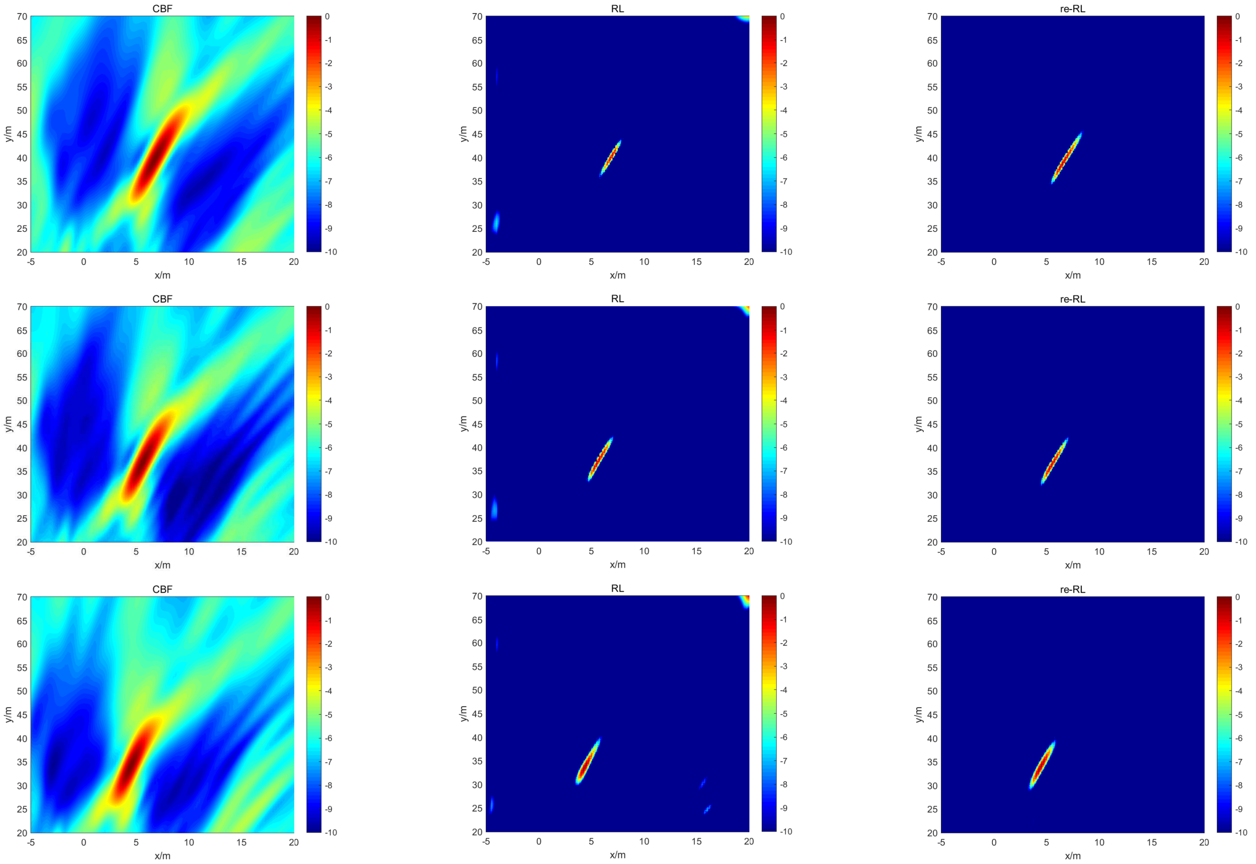

(a) CBF (b) RL (c) re-RL

Fig. 15: UAI of single source

is slightly larger than that of the RL algorithm, and the sidelobe levels between them are close though that of the former is slightly lower than that of the latter; these observations are consistent with the simulation results. The images obtained by the non-uniform spatial resampling RL algorithm are close to images obtained by the original RL algorithm, but the former requires significantly less computational effort due to a smaller number of grid points as Table 5 shows. The computational complexity of the re-RL method is 15 times lower than that of the RL method.

The processing results for the CBF, RL, and re-RL algorithms with 100 deconvolution iterations for two different moving source positions of dual-sources are shown in Fig. 16. The spacing between the two sources was about 20 m. The signal processing frequency range in this case was from 300Hz to 500 Hz. The partition parameters are listed in Table 6.

Table 6 Subsets of spatial resampling for the experiment with two sources

i	Threshold D_i	k_i
1	0dB	1
2	-3dB	5
3	-6dB	10

Table 7 shows the number of scan points in the two RL methods with a uniform grid sampling interval of 0.5 m×1m (the sampling interval over the x-axis is 0.5m, and over the y-axis is 1m) as an example.

As shown in Fig.16, the sidelobe level of the RL and re-RL algorithms are significantly lower than that of the conventional acoustic image. The mainlobe area of the re-RL algorithm is slightly larger than that of the RL algorithm, and the sidelobe levels between them are close though that of the former is slightly lower than that of the latter; these observations are consistent with the simulation results. It can be seen from Table 7 that the number of scan points in the case of dual-source drops less than in the case of the single source, because its sidelobe level is too high to use the high-power downsampling area.

Table 7 Comparison of the number of scan points

Sampling method Sound positions	Uniform sampling	Non-uniform sampling
Position 1	14241	3655
Position 2	14241	3558

7 Conclusion

This paper presented a fast RL deconvolution algorithm for 2D PSF shift-variant model; it is based on spatial resampling. We designed this method to minimize the computational burden of the traditional deconvolution process for the robust high-resolution passive location of underwater sources. The theoretical and simulation analysis indicate that the spatial resampling RL method maintains the convergence of the original RL algorithm. Simulations showed that the proposed method performs similarly to the original RL algorithm with a markedly lower computational burden (nearly one order of magnitude). The mainlobe area of the spatial resampling RL algorithm is slightly higher than that of the original RL algorithm (though very similar). The limit resolution of the RL and spatial resampling RL algorithms are very close. The sidelobe level of the spatial resampling RL algorithm is slightly lower than that of the original RL algorithm for SNRs between of -10dB and 5dB. We

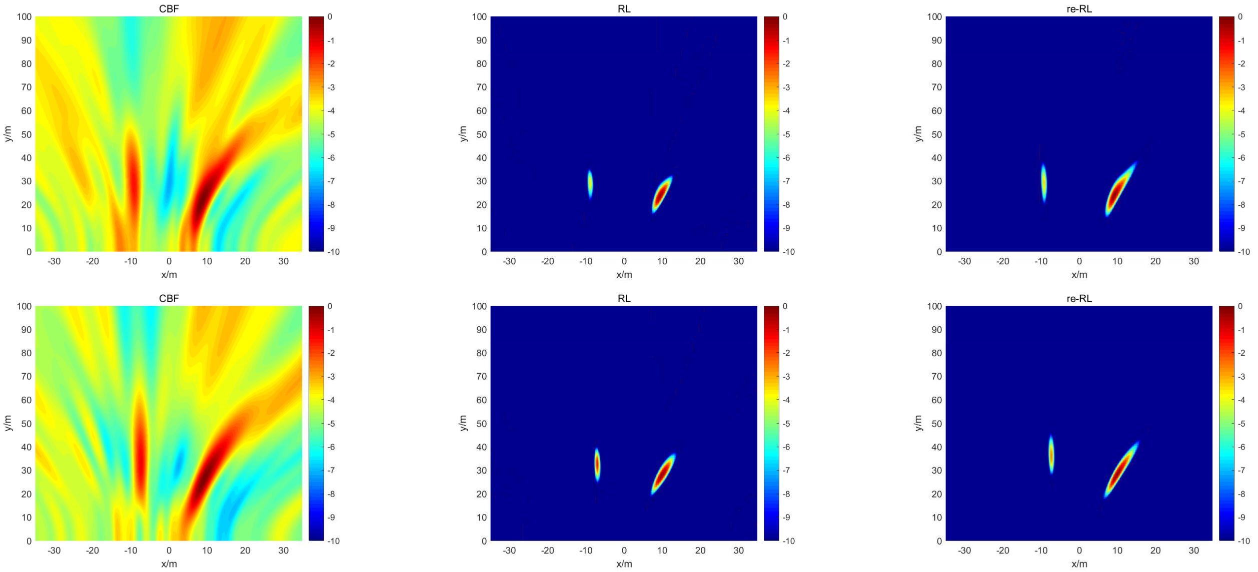

(a) CBF (b) RL (c) re-RL

Fig. 16: UAI of dual-source

took the position errors of the array elements as an example to illustrate the robustness of the proposed method. The results show that the original RL and the fast RL deconvolution algorithms have high robustness and are not very sensitive to small position errors of the array elements, since both the original UAI and PSF dictionary generation are based on CBF and CBF possesses a high robustness. Results of a sea trial indicate that the mainlobe area of the re-RL algorithm is slightly larger than that of the RL algorithm, and the sidelobe levels between them are fairly close though that of the former is slightly lower than that of the latter; these observations are consistent with the simulation results. The next step of the research is how to reasonably choose the threshold and the sampling rate, so as to improve the calculation speed and obtain the required results at the same time.

8 Acknowledgments

This work was supported by the National Natural Science Foundation of China under Grants 61801140 and 61701132, Natural Science Foundation of Heilongjiang Province under Grants YQ2019D003. And the work of Y. Zakharov was supported in part by the U.K. EPSRC Grants EP/P017975/1 and EP/R003297/1.

9 References

1 Kim K M , Yang I S , Chun S Y , et al. Passive-range estimation using dual focused beamformers. IEEE Journal of Oceanic Engineering, 2002, 27(3):638-641P.
2 Jie, Shi, Bosheng Liu, et al. Radiated noise sources location based on MVDR near-field focused beamforming. IEEE Conference on Industrial Electronics & Applications, Singapore, June 2008.
3 Kino, G., ed. (2000). Acoustic Waves: Devices, imaging, and analog signal processing. Prentice Hall. Chapter3, page 165.
4 J.Capon. High-resolution frequency-wavenumber spectrum analysis. Proc. IEEE, 1969, 57(8):1408-1418P.
5 Schmidt R O. Multiple emitter location and signal parameter estimation. IEEE Trans. Antennas Propagate., 1986, 34(3):276-280P.
6 Roy R, Paulraj A, Kailath T. ESPRITÍCA subspace rotation approach to estimation of parameters of cissoids in noise. IEEE Transactions on Acoustics Speech & Signal Processing, 1986, 34(5):1340-1342P.
7 Earl G. Williams, J D Maynard, Eugen Skudrzyk. Sound source constructions using a microphone array. The Journal of the Acoustical Society of America, 1980, 68(1):340-344P.
8 E. Tiana-Roig, F. Jacobsen. Deconvolution for the localization of sound sources using a circular microphone array. The Journal of the Acoustical Society of America,2013, 134(3):2078-2089P.
9 Peng Shao, Mengdao Xing, Xiang-Gen Xia. Autofocus algorithm using blind homomorphic deconvolution for synthetic aperture radar imaging. IET Radar Sonar & Navigation, 2015, 9(7):900-906P.
10 Xenaki A, Jacobsen F, Fernandez-Grande E. Improving the resolution of three-dimensional acoustic imaging with planar phased arrays. Journal of Sound & Vibration, 2012, 331(8):1939-1950P.
11 R. E. Blahut. Theory of Remote Image formation. Cambridge Univ. Press, 2004, Ch. 9 and 11.
12 T. C. Yang. Deconvolved conventional beamforming for a horizontal line array. IEEE J. Ocean. Eng., 2018, 43(1):160-172P.
13 T. C. Yang. Performance analysis of superdirectivity of circular arrays and implications for sonar systems. IEEE J. Ocean. Eng., 2018, 44(1):156-166P.
14 Dougherty R P. Extensions of DAMAS and Benefits and Limitations of Deconvolution in Beamforming. 11th AIAA/CEAS Aeroacoustics Conference, Monterey, California, May 23-25, 2005.
15 Smaragdis P. Non-negative matrix factor deconvolution; extraction of multiple sound sources from monophonic inputs. Proc Ica, 2004, 3195:494-499P.
16 Bose R, Freedman A, Steinberg B D. Sequence CLEAN: a modified deconvolution technique for microwave images of contiguous targets. IEEE Transactions on Aerospace and Electronic Systems, 2002, 38(1):89-97P.
17 W. H. Richardson. Bayesian-based iterative method of image restoration. J. Opt. Soc. Amer., 1972, 62:55-59P.
18 L. B. Lucy. An iterative technique for the rectification of observed distributions. Astron. J., 1974, 79:745-754P.
19 Bertero M, Boccacci P. A simple method for the reduction of boundary effects, in the Richardson-Lucy approach to image deconvolution. Astronomy and Astrophysics, 2005, 437(1):369-374P.
20 Yardibi T, Li J, Stoica P, et al. Sparsity constrained deconvolution approaches for acoustic source mapping. Journal of the Acoustical Society of America, 2008, 123(5):2631-2642P.
21 Tianaroig E, Jacobsen F. Deconvolution for the localization of sound sources using a circular microphone array. Journal of the Acoustical Society of America, 2013, 134(3):2078-2089P.
22 Lylloff OFernandez-Grande EAgerkvist Fet al. Improving the efficiency of deconvolution algorithms for sound source localization . Journal of the Acoustical Society of America, 2015, 138(1):172-180P.
23 Ehrenfried K, Koop L. Comparison of Iterative Deconvolution Algorithms for the Mapping of Acoustic Sources. AIAA Journal, 2007, 45(7):1-19P.
24 Bo Zhao, Wensheng Zhang, Huan Ding. A new algorithm for image deblurring based on Richardson-Lucy. Computer Engineering and Applications, 2011, 47(34):1-4P.
25 Zhigang Chu, Yang Yang, Yansong He. Deconvolution for three-dimensional acoustic source identification based on spherical harmonics beamforming. Journal of Sound & Vibration, 2015, 344:484-502P.
26 Dajun Sun, Chao Ma, T. C. Yang, et al. Improving the Performance of a Vector Sensor Line Array by Deconvolution[J]. IEEE Journal of Oceanic Engineering, DOI: 10.1109 /JOE. 2019.2912586. (in press)
27 Jidan Mei, Wenpei Shi, Chao Ma, Dajun Sun. Near-field focused beamforming acoustic image measurement based on deconvolution. ACTA ACUSTICA. 2020, 45(1):15-28P.
28 Dajun Sun, Chao Ma, Jidan Mei, et al. Improving the resolution of underwater acoustic image measurement by deconvolution. Applied Acoustics, v165, August 2020.
29 Liang Zhang, Jidan Mei, Adam Zielinski, Ping Cai. Accurate Acoustic Signal Parameter Estimation for Marine Geodesy Surveys. Marine Geodesy. 2018
30 D. L. Snyder, T. J. Schulz, A. O'Sullivan. Deblurring subject to nonnegativity constraints. IEEE Trans. Signal Process., 1992, 40(5): 1143ÍC1150P.
31 J. A. O'Sullivan, R. E. Blahut, D. L. Snyder. Information-theoretic image formation. IEEE Trans. Inf. Theory, 1998, 44(6):2094-2123P.